Astronomy & Astrophysics manuscript no. papII˙v18
November 8, 2012
© ESO 2012

arXiv:1211.1546v1 [astro-ph.SR] 7 Nov 2012

Seismic diagnostics for transport of angular momentum in stars

2. Interpreting observed rotational splittings of slowly-rotating red giant stars

M.J. Goupil[1], B. Mosser[1], J.P. Marques[2,1], R.M. Ouazzani[3,1], K. Belkacem[1], Y. Lebreton[4], and R. Samadi[1]

[1] LESIA, CNRS UMR 8109, Université Pierre et Marie Curie, Université Denis Diderot, Observatoire de Paris, F-92195 Meudon, France;
[2] Georg-August-Universität Göttingen, Institut für Astrophysik, Friedrich-Hund-Platz 1, D-37077 Göttingen, Germany
[3] Institut d'Astrophysique, Géophysique et Océanographie de l'Université de Liège, Allée du 6 Août 17, 4000 Liège, Belgium
[4] Observatoire de Paris, GEPI, CNRS UMR 8111, F-92195 Meudon, France

Preprint online version: November 8, 2012

ABSTRACT

Asteroseismology with the space-borne missions CoRoT and *Kepler* provides a powerful mean of testing the modeling of transport processes in stars. Rotational splittings are currently measured for a large number of red giant stars and can provide stringent constraints on the rotation profiles.
The aim of this paper is to obtain a theoretical framework for understanding the properties of the observed rotational splittings of red giant stars with slowly rotating cores. This allows us to establish appropriate seismic diagnostics for rotation of these evolved stars.
Rotational splittings for stochastically excited dipolar modes are computed adopting a first-order perturbative approach for two $1.3 M_{\odot}$ benchmark models assuming slowly rotating cores.
For red giant stars with slowly rotating cores, we show that the variation of the rotational splittings of $\ell = 1$ modes with frequency depends only on the large frequency separation, the g-mode period spacing, and the ratio of the average envelope to core rotation rates ($\mathcal{R}$). This leds us to propose a way to infer directly $\mathcal{R}$ from the observations. This method is validated using the Kepler red giant star KIC 5356201. Finally, we provide a theoretical support for the use of a Lorentzian profile to measure the observed splittings for red giant stars.

Key words. star:evolution- stars: interiors- stars: rotation- stars: oscillations

1. Introduction

Stellar rotation plays an important role on the structure and evolution of stars. The problem of transport of angular momentum inside stars is not yet fully understood, however. Several mechanisms seem to be active although they are either only approximately described or not modeled at all. In order to study the internal transport and evolution of angular momentum with time, one needs observational constraints on physical quantities affected by such transport processes. In particular, the knowledge of the internal rotation profiles and their evolution with time is crucial. An efficient way is to obtain seismic information on the internal rotation profile of stars.

The ultra-high precision photometry (UHP) asteroseismic space missions such as CoRoT (Baglin et al. 2006) and *Kepler* (Borucki et al. 2010) offer such an opportunity. Because cool low-mass stars have a convective envelope, oscillations can be stochastically excited as in the solar case. Red giant stars are of particular interest here. Stochastically excited non-radial modes were detected with CoRoT (De Ridder et al. 2009). Analyses of these data revealed the oscillation properties of a large number of these stars (e.g., Hekker et al. 2009; Mosser et al. 2010, 2011a; Bedding et al. 2011). Their frequency spectra show similarities as well as differences with the solar case (Mosser et al. 2011b). Several works have investigated the properties of the non-radial oscillation modes of red giant stars (e.g., Osaki 1975; Dziembowski 1977; Dziembowski et al. 2001; Dupret et al. 2009; Montalbán et al. 2010). The internal properties of a red giant star, a dense core and a diffuse envelope, give rise to both gravity-type oscillations in the central region and acoustic-type oscillations in the envelope. These oscillations were first called mixed modes by Dziembowski (1971) for a Cepheid model and Scuflaire (1974) for condensed models representative of a red giant structure. This has already been proved useful to probe the structure of these stars (e.g., Bedding et al. 2011; Mosser et al. 2011a).

More recently, measurements of rotational splittings of red giant stars have been obtained by using the *Kepler* observations (e. g., Deheuvels et al. 2012; Beck et al. 2012; Mosser et al. 2012b). These splittings provide the first direct insight into the rotation profiles of the innermost layers of stars (Deheuvels et al. 2012). Observations (Mosser et al. 2012a) reveal that a sub-sample of oscillating red giants have complex frequency spectra. Their central layers are likely to rotate quite fast. A correct rotation rate ought then be deduced from direct calculations of frequencies in a non-pertubative approach (see the case for polytropes and acoustic modes in Reese et al. 2006; Lignières 2011; Ouazzani et al. 2012 and for g modes in Ballot et al. 2010, 2011). This will be necessary in order to decipher

the complex spectra for fast rotation. On the other hand, the rest of the sample shows simple power spectra that can be easily identified without ambiguity. These identifications then lead to quite small rotational splittings (Beck et al. 2012; Mosser et al. 2012a), thus to slowly rotating cores.

On the theoretical side, the central rotations predicted theoretically by standard models currently including rotationally induced mixing are far too fast (e.g., Eggenberger et al. 2012) and cannot account for these observed slow core rotation in red giants.

Motivated by these recent results, we have started a series of studies dedicated to an understanding of the rotational properties of oscillating evolved stars. Marques et al. (2012) (hereafter Paper I) computed the rotation profiles and their evolution with time from the pre main-sequence to the red giant branch (RGB) for 1.3 $M_\odot$ stellar models with an evolutionary code where rotationally induced mixing had been implemented. The authors then followed the evolution of the rotational splittings calculated to first-order approximation in the rotation rate using the rotation profiles predicted by their evolutionary computations. The authors found that for low-mass stars, the first-order approximation is valid for most stochastically excited oscillation modes for all evolutionary stages except the RGB. For red giants, the authors showed that there is indeed room enough in the uncertainties of the description of transport of angular momentum to decrease significantly the core rotation of red giant models (see also Meynet et al. 2012). However, they still predict a core rotation that is still too large compared with the observed rotational splittings, meaning that some additional processes are operating in the star to slow down its core. To test such possible additional mechanisms, investigations of the specific properties of the rotational splittings of red giants with slow core rotation must be carried out, essentially because of the particular dual nature of the excited red giant modes.

We thus defer the study of red giants with fast rotating cores to the third paper of this series. We focus here on red giants with slowly rotating cores. We present a study of the properties of linear rotational splittings, computed for adiabatic oscillation modes, in the frequency range of observed modes in red giant stars. We assume arbitrarily slow rotation profiles and then study essentially the impact of the properties of the modes on the rotational splittings. Our goal is to provide a theoretical framework for the interpretation of the observed rotational splittings of red giants in terms of core and envelope rotation.

The paper is organized as follows; in Sect. 2, we describe the properties of our models. In order to interpret the rotational splittings, we need first to identify the physical nature of the excited modes. This is done in Sect. 3 where we distinguish two classes of mixed modes. In Sect. 4, we compute theoretical rotational splittings using adiabatic eigenfrequencies and eigenfunctions obtained for $\ell = 1$ modes. The studied frequency range corresponds to expected stochastically excited modes. We then show that the rotational splittings exhibit repetitive patterns with frequency that can be folded into a single pattern as they carry nearly the same information. We then consider in detail such pattern for one of our models and investigate the information provided by the corresponding rotational splittings. In Sect. 5, we establish an approximate formulation for the linear rotational splittings in terms of the core contribution to mode inertia. The approximate expression fits well the numerical ones and allows us their interpretation. We also give a procedure that enables ones to derive the mean rotation of the core and of the envelope. Proceeding further in the approximations in Sect.6, we find an approximate formulation of the core contribution to mode inertia – thus to rotational splittings – that depends only on observable quantities aside rotation. We validate our theoretical results on the Kepler observations of the star KIC 5356201 (Beck et al. 2012). Finally, we end with some conclusions in Sect.8.

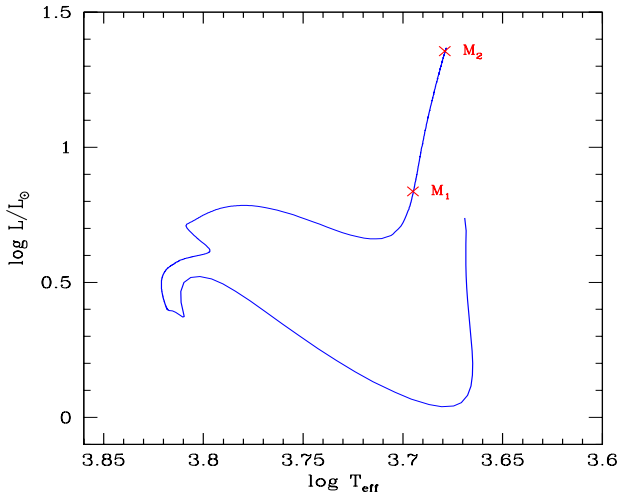

Fig. 1. Hertzsprung-Rüssell (HR) diagram showing a $1.3M_\odot$ evolutionary track. The red crosses indicate the selected models as described in Sect. 2 and in Table. 1.

Table 1. Fundamental parameters of the 1.3 $M_\odot$ stellar models.

model	M1	M2
$R/R_\odot$	3.58	6.91
$\log T_{\rm eff}$ (K)	3.694	3.758
$\log L/L_\odot$	0.825	1.345
ρ_c (10^7 kg/m^3)	7.06	14.05
$\rho_c/\bar{\rho}$ (10^6)	5.12	75.85
$r_{CZ}(m_{CZ})$	0.25 (0.33)	(0.078) (0.197)
$r_\epsilon(m_\epsilon)$	0.01 (0.13)	($4.5\ 10^{-3}$) (0.168)
$\Delta\nu$ (μHz)	23.12	8.47
$\Delta\Pi$ (s)	96.64	71.14
$\nu_{\rm max}$ (μHz)	342.6	83.5
$n_{\rm max}$	14	9

2. Structures of stellar models and rotation profiles

We consider $1.3M_\odot$ models of red giants as this mass is typical for observed red giant stars (Mosser et al. 2010). These models (structure and rotation profile) have been evolved from PMS as described in Paper I.

2.1. Selected models

The first model (M1) lies at the base of the red giant branch (Fig. 1). Its outer convective zone occupies 67 % in mass of the outer envelope and is located at $\Delta m/M = 0.2$ above

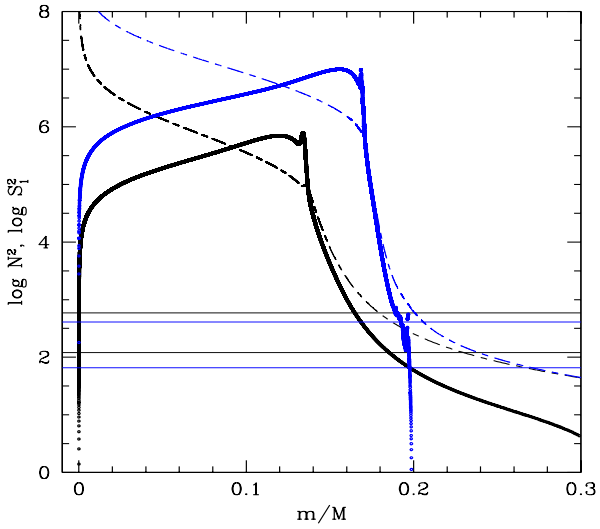

Fig. 2. Logarithm of normalized squared Brunt-Väisälä N^2 (solid curve) and ($\ell = 1$) Lamb frequencies S_l^2 (dash-dotted curve) as a function of the normalized mass m/M for model M1 ($\log_{10}\sigma^2_{\rm max} = 2.60$) (black curves) and M2 ($\log_{10}\sigma^2_{\rm max} = 2.32$) (blue curves). The thin horizontal solid lines indicate the frequency range for expected excited oscillation modes: black for model M1 and blue for M2.

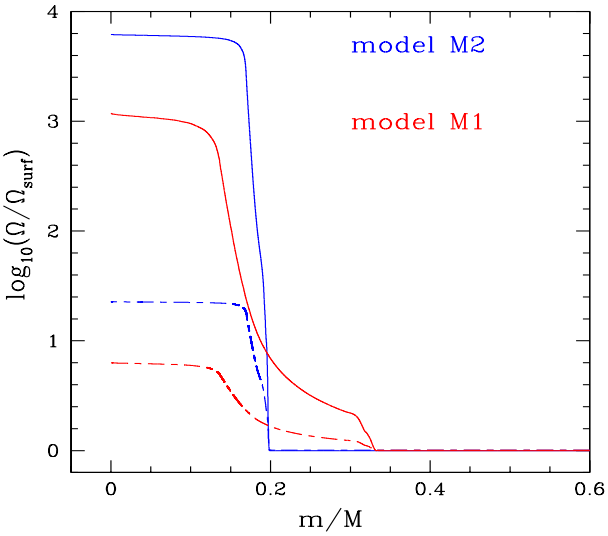

Fig. 3. Rotation profiles as a function of the normalized mass. The surface values are $\mathbf{\Omega}_{\rm surf}/(2\pi) = 0.154, 0.042$ $\boldsymbol{\mu}$Hz respectively. Original Ω profiles stemmed from the evolution of the stellar models (red solid curve for model M1 and blue solid curve for model M2). The dot-dashed lines represent the rotation profiles that have been arbitrarily decreased by assuming $\Omega_{\rm surf}(\Omega/\Omega_{\rm surf})^{1/f}$ with $f = 3.85$ for model M1 (red curve) and $f = 2.8$ for model M2 (blue curve).

the H-shell burning. The second model (M2) is further up on the ascending branch (Fig.1). Its outer convective zone occupies 80 % of the outer envelope and is at $\Delta m/M = 0.015$ above the H-shell burning. Table 1 lists the stellar radius in solar unit, the effective temperature, luminosity in solar unit, the central density ρ_c, the ratio $\rho_c/\bar{\rho}$ with $\bar{\rho} = 3M/(4\pi R^3)$, the radius at the base of the outer convective zone, the radius of maximum nuclear production rate, both normalized to the stellar radius, the seismic quantities: the large separation $\Delta\nu$, the g mode period spacing $\Delta\Pi$ (in s), the frequency at maximum power spectrum intensity $\nu_{\rm max}$, the radial order $n_{\rm max}$ at $\nu_{\rm max}$.

The propagation diagrams (Osaki 1975) for models M1 and M2 are displayed in Fig. 2. Only the central part is shown as it plays a major role in determining the properties of the oscillation modes of red giants (see Sect. 3). The Brunt-Väisälä (N) and Lamb (S_ℓ) frequencies take their usual definition, *i.e.*,

$$N^2 = \frac{g}{r}\left(\frac{1}{\Gamma_1}\frac{{\rm d}\ln p}{{\rm d}\ln r} - \frac{{\rm d}\ln\rho}{{\rm d}\ln r}\right), \quad (1)$$

$$S_\ell^2 = \frac{\Lambda c_s^2}{r^2}, \quad (2)$$

where $\Lambda = \ell(\ell+1)$, ℓ is the angular degree of the mode, c_s^2 is the squared sound speed, the gravity $g = Gm/r^2$, and p, ρ, Γ_1 have their usual meaning. Unless otherwise stated, we consider all squared frequencies N^2, S_ℓ^2 to be normalized to GM/R^3 and $\sigma^2 = \omega^2/(GM/R^3)$ (where ω is the mode pulsation in rad/s).

Model M2 is more evolved and more centrally condensed than M1. Accordingly, the inner maximum of the Brunt-Väisälä frequency is higher than for the younger model M1 (Montalbán et al. 2010) and N decreases more sharply. The range of frequency corresponding to the expected excited modes are indicated by horizontal lines. They show that the evanescent region between the inner g resonant cavity and the upper p resonant cavity (*i.e.*, between the Brunt-Väisälä and Lamb frequencies) is quite narrow for these modes.

2.2. Rotation profiles

The original rotation profiles obtained for models M1 and M2 from evolution are displayed in Fig. 3. The central regions of the more evolved model M2 are rotating much faster than those of M1 (amounting to 181.5 and 260 μHz respectively). With such high rotation rates, we checked first that the centrifugal acceleration is negligible compared to local gravity in our models (that is, with a relative magnitude of 10^{-4} at most). We can therefore still safely assume a spherically symmetric equilibrium state. However, the linear approximation is no longer valid due to Coriolis effects when $2\Omega/\omega$ is close to unity. This happens in the central regions of the models for the modes we consider. As we study here slowly rotating red giants, we assumed that some slowing down process has and/or is occurring in real stars that are not yet included in our models. We therefore artificially decrease the rotation rates stemmed from our evolutionary models so that the first-order approximation for the rotational splittings is valid. The shape of the rotation profile due to slowing down is unknown, we therefore keep it unchanged and investigate whether this can be confirmed or not by confrontation with observations.

We therefore decrease the central rotation rates by rescaling the rotation profile stemmed from our evolution-

ary models, decreasing the central values but keeping the same envelope rotation rate. The decrease is set so that the value of the computed rotational splittings agree with observed ones. For instance, for model M1, the initial central rotation, 181.5 μHz, is decreased down to 0.967 μHz. The rotation profiles we use to compute the linear rotational splittings in the following sections are then shown in Fig. 3.

3. Classification of mixed modes

The rotational splittings depend not only on the rotation profile but also on the eigenfunctions – that is on the physical nature – of the excited modes. Stellar models of red giant stars exhibit an outer convective region that is able to efficiently drive modes stochastically (Samadi et al. 2012). Thus, we consider the frequency ranges for our models that span an interval of a few radial orders below and above $n_{\rm max}$ (the radial order corresponding to the frequency at maximum power). We estimate $n_{\rm max}$ as $n_{\rm max} = \nu_{\rm max}/\Delta\nu$, where the frequency at maximum power spectrum $\nu_{\rm max}$ and the mean large separation $\Delta\nu$ are given by the usual scaling relations (e.g., Kjeldsen & Bedding 1995)

$$\nu_{\rm max} = \nu_{\rm max,\odot} \left(\frac{M}{M_\odot}\right) \left(\frac{R}{R_\odot}\right)^{-2} \left(\frac{T_{\rm eff}}{T_{\rm eff,\odot}}\right)^{-1/2}, \quad (3)$$

$$\Delta\nu = \Delta\nu_\odot \left(\frac{M}{M_\odot}\right)^{1/2} \left(\frac{R}{R_\odot}\right)^{-3/2}, \quad (4)$$

with $T_{\rm eff,\odot} = 5777$ K and the reference asymptotic values $\nu_{\rm max,\odot} = 3106\,\mu$Hz, and $\Delta\nu_\odot = 138.8\,\mu$Hz defined and calibrated by Mosser et al. (2013). Indeed, it has been conjectured by Brown et al. (1991), then shown observationally by Bedding & Kjeldsen (2003), that $\nu_{\rm max}$ predicts well the location of the excited frequency range of stochastically excited modes. A physical justification has been recently proposed by Belkacem et al. (2011). The adiabatic oscillation frequencies and eigenfunctions for $\ell = 1$ modes are computed with the ADIPLS code (Christensen-Dalsgaard 2008).

As expected from previous works (e.g., Osaki 1975; Dziembowski 1977; Dziembowski et al. 2001; Dupret et al. 2009; Montalbán et al. 2010), our red giant models show many mixed $\ell = 1$ modes. For model M1, for instance, the frequency range of excited modes is expected to be $\log_{10}(\sigma^2) \sim 2 - 2.8$. For modes that are expected to be excited around ν_max (given in Table 2), the corresponding frequencies are much smaller than both the Brunt-Väisälä frequency and the Lamb frequency in the central regions of the models (see Fig. 2). Therefore, modes with frequencies close to ν_{max} are trapped in the g resonant cavity, located in the radiative central region. Moreover, $\sigma^2_{\rm max} \gg N^2, S^2_\ell$ in most of the envelope so that the modes are also trapped in the p resonant cavity in the convective envelope (not shown). These cavities boundaries are delimited by turning points, i.e. the radii satisfying $\sigma^2 = N^2(r)$ (g cavity bounded by x_1 and x_2), or $\sigma^2 = S^2_\ell(r)$ (p cavity bounded by x_3 and x_4). The location of these turning points for a list of selected modes are given in Sect. 4-1, Table 3.

In order to interpret correctly the observed rotational splittings, we need to define a measure of the g nature of the modes with respect to their p part and classify them accordingly. Convenient quantities for that purpose

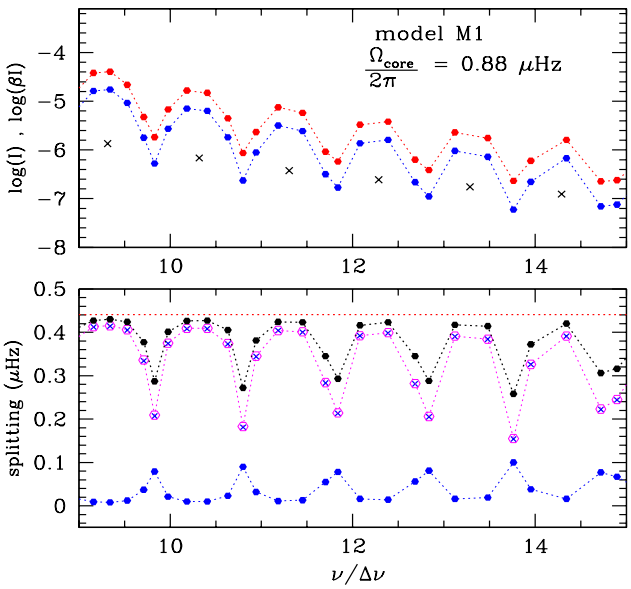

Fig. 4. *Top:* Integrated kernel (β I) with β and I respectively given by Eq. 13 and Eq. 8 (blue dotted line, dots correspond to modes) and mode inertia I (red dotted line, dots correspond to modes) in decimal logarithm for model M1. Black crosses represent the inertia of radial modes. *Bottom:* Rotational splittings (Eq.11), in μHz, for $\ell = 1$ modes as a function of the normalized frequency $\nu/\Delta\nu$ for M1 (black dots connected by a dotted line). Dotted blue and magenta curves and blue crosses represent various contributions and approximations to the rotational splittings (see text Sect.5). The value $(1/2)\langle\Omega\rangle_{\rm core}/2\pi$ is represented by the horizontal red dotted line.

are the kinetic energy (Unno et al. 1989) or the mode inertia (Dziembowski et al. 2001), defined as

$$\mathcal{I} = 4\pi R^3 \int_0^1 \left(\xi_{\rm r}^2 + \Lambda\xi_{\rm h}^2\right) \rho\, x^2\, {\rm d}x\,, \quad (5)$$

with $\Lambda = \ell(\ell+1)$, and $x = r/R$ is the normalized radius. The oscillation quantities entering the above definition are the fluid vertical and horizontal displacement eigenfunctions $\xi_{\rm r}, \xi_{\rm h}$ respectively. For later convenience, we will use the following variables

$$z_1 = \left(\frac{3\rho}{\bar\rho}\right)^{1/2} x^{3/2}\, \frac{\xi_{\rm r}}{R}\,, \quad (6)$$

$$z_2 = \sqrt{\Lambda} \left(\frac{3\rho}{\bar\rho}\right)^{1/2} x^{3/2}\, \frac{\xi_{\rm h}}{R}\,. \quad (7)$$

Using Eqs. (6) and (7) into (5) leads to (dropping the subscripts n, ℓ)

$$I = \int_0^1 \left(z_1^2 + z_2^2\right) \frac{{\rm d}x}{x}\,, \quad (8)$$

where we have defined the dimensionless mode inertia I as $I = \mathcal{I}/(MR^2)$.

The variation of $\ell = 1$ mode inertia with frequency is shown in Figs. 4 and 5 for models M1 and M2. The number

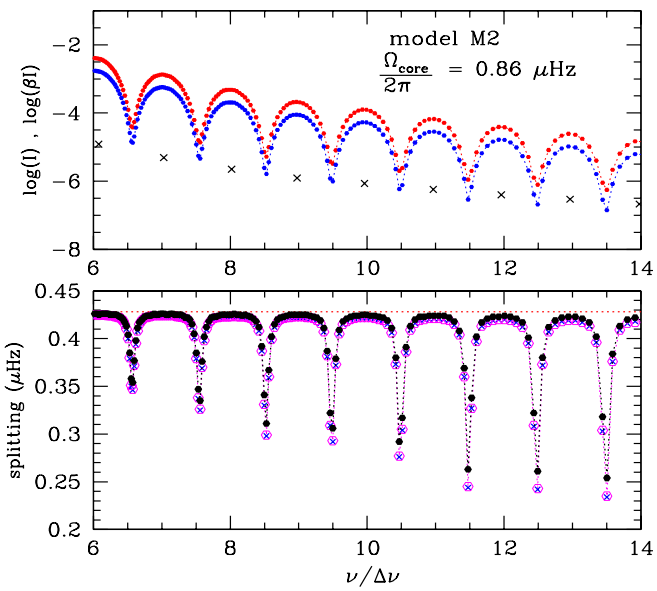

Fig. 5. Same as Fig. 4 but for model M2.

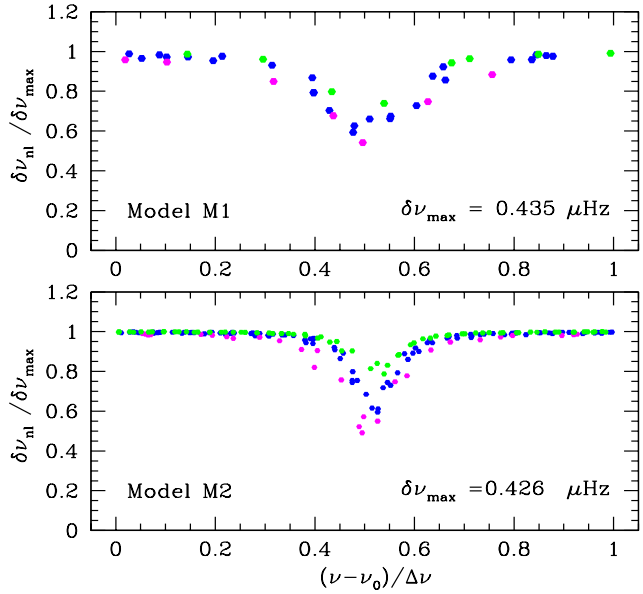

Fig. 6. Folded rotational splittings according to $(\nu - \nu_0)/\Delta\nu$ for *Top:* model M1 (blue $9 < \nu/\Delta\nu < 15$; magenta $\nu/\Delta\nu > 15$; green $\nu/\Delta\nu < 9$) and *Bottom:* for model M2 (blue $8 < \nu/\Delta\nu < 14$; magenta $\nu/\Delta\nu > 14$; green $\nu/\Delta\nu < 8$). The splittings are normalized to their maximum values, which are written in the panels.

of nodes in the g cavity is given by

$$n_g = \frac{\sqrt{\Lambda}}{\pi\omega} \int_{\rm core} \frac{N}{x}\, dx\,, \qquad (9)$$

(Unno et al. 1989, and references therein).

Because N^2 increases with evolution (see Fig. 2 for M1 and M2), the number of nodes, hence of modes, in a given frequency range increases with the age of the star. This can be seen by comparing Fig. 4 for model M1 and Fig. 5 for model M2. Mixed modes with a g-dominated character have their inertia larger than modes that have their inertia shared between the g and p cavities. These results are in agreement with previous works (e.g., Dupret et al. 2009).

We now define for convenience a measure of the g nature of the mode with the ratio of mode inertia in the g cavity over the total mode inertia (Deheuvels et al. 2012), *i.e.*,

$$\zeta = \frac{I_{\rm core}}{I} = \frac{1}{I}\int_0^{r_{\rm core}} (z_1^2+z_2^2)\,\frac{{\rm d}x}{x} \sim \frac{1}{I}\int_0^{r_{\rm core}} z_2^2\,\frac{{\rm d}x}{x}\,. \quad (10)$$

For a mode with a p-dominated nature, the inertia is concentrated in the p-cavity and is small due to the low density in the envelope ($\zeta \sim 0$). Its frequency is mainly determined by the p-cavity and is therefore half a large separation away from the frequencies of consecutive radial modes.

For a mixed mode where the g character dominates ($\zeta \sim 1$), the inertia is large due to the high density of the central regions where the mode has its maximum amplitude. The frequency of this $\ell = 1$ mixed mode differs significantly from that of a $\ell = 1$ mode that would be a pure p mode. Its frequency is then closer to that of the closest radial mode. We refer later to such a mode as a *g-m mode* as in Mosser et al. (2012a).

When the contributions to mode inertia from the core and the envelope are nearly equal, the mode frequencies are less affected by the core and therefore remain closer to the frequencies of pure $\ell = 1$ p modes. We will refer to such mixed modes as *p-m modes* (Mosser et al. 2012a). These modes take intermediate values of ζ.

4. Linear rotational splittings

For slow rotation, a first-order perturbation theory provides the following expression for the rotational splittings (Ledoux 1951; Christensen-Dalsgaard & Berthomieu 1991)

$$\delta\nu = \int_0^1 K(x)\,\frac{\Omega(x)}{2\pi}\,{\rm d}x\,, \qquad (11)$$

where Ω is the angular rotation velocity and the rotational kernel K takes the form

$$K = \frac{1}{I}\Big(z_1^2 + z_2^2 - \frac{2}{\sqrt{\Lambda}} z_1\, z_2 - \frac{1}{\Lambda}\, z_2^2\Big)\,\frac{1}{x} \qquad (12)$$

normalized to the mode inertia I. For later purpose, we also define

$$\beta = \int_0^1 K(x)\,{\rm d}x\,. \qquad (13)$$

We compute the rotational splittings according to Eq. (11) for $\ell = 1$ modes and will refer to them as numerical rotational splittings later on. The variations of the rotational splittings with the normalized frequency $\nu/\Delta\nu$ are shown for model M1 an M2 in Figs. 4 and 5. Also displayed are the variations of both the inertia I and the product $\beta\, I$ (with β and I respectively given by Eq. 13 and Eq. 8). They show that the oscillatory variations of the splittings with frequency are dominated by the nature of the modes as they closely follow those of mode inertia and of the integrated kernel $\boldsymbol{\beta}\,\mathbf{I}$ (see Sect. 4.2).

It may be useful to the reader to note that models that are located at the same location in the HR diagram (models with the same mass but one with an overshoot of 0.1 pressure scale height and no rotational induced mixing and one without overshoot but with rotational induced mixing) have similar structures. As a consequence, the rotational splitting of any given mode in the range of interest here is the same for both models when computed with the eigenfunctions of the respective models and the same rotation profile.

4.1. Periodic patterns for rotational splittings

It is clear from Fig. 4 and 5 that the variation of the mode inertia and rotational splitting with frequency shows a quasi-periodic pattern, with a period close to the large separation. Each pattern around a radial mode carries roughly the same information about the rotation, at least in the range of observed modes for red giants as found by Mosser et al. (2012a). Note, however, that at higher frequencies, mixed modes become closer to pure p modes and probe the rotation of the surface layers, while at lower frequency, the nature of g-m modes is much closer to that of pure g modes and probe better the inner rotation.

The existence of repeated patterns leads us to gather information by folding the power spectrum according to the large separation $\Delta\nu$. The rotational splittings are plotted, in Fig. 6, as a function of $(\nu-\nu_0)/\Delta\nu$ where ν_0 is the closest radial mode to the $\ell=1$ mode of frequency ν. The folding $(\nu-\nu_0)/\Delta\nu$ corresponds to the asymptotic folding $\nu/\Delta\nu-(n_p+\varepsilon)$ as suggested by Mosser et al. (2012b), where n_p is the radial order of the mode and ε represent some departure from the asymptotic description (Tassoul 1980; Mosser et al. 2012a). This folding is shown for our two models in Fig. 6. We see that all patterns do nearly superpose for each model. Here $\varepsilon\sim 1.3-1.4$ for model M1 and $\varepsilon\sim 0$ for model M2. A clear correlation exists between the magnitude of the splitting and the g nature of the mixed mode. The rotation splittings are large for g-m modes that lie on the left and right sides of a minimum occupied by the p-m modes that have the smallest rotation splittings. This is in agreement with recent observations (Mosser et al. 2012b). In the low-frequency domain, the modes are, for most of them, g-m modes. At higher frequency, they can be either g- or p-m modes (Fig. 6). This is clearly seen when one looks at restricted domains of frequency (corresponding to different color codes in Fig.6).

We also note that the ratio of the minimum splittings $\delta\nu_{\rm min}$ to the maximum ones $\delta\nu_{\rm max}$ (~ 0.5 for for model M1 and M2) is only slightly sensitive to rotation. Actually, it depends only on the ratio of the envelope to core rotation which is small. This is explained in Sect.6.

4.2. Properties of a periodic pattern

To interpret the behavior of the splittings, we consider a single pattern around a given $\ell=0$ mode with radial-order $n_p=10$ (Table 2) for model M1. There are six modes in the pattern labelled ν_1 to ν_6 from the smallest to the largest frequency.

Table 2. Model M1 frequencies of the selected pattern: the frequency ν in μHz, $\boldsymbol{\sigma}$ is the normalized frequency $2\pi\nu(GM/R^3)^{-1/2}$, I is the mode inertia arbitrarily normalized to mode inertia of the radial mode $n=8$; $\zeta=I_{\rm core}/I$

			$\ell=0$		
n_p	ν	σ^2	$\nu/\Delta\nu$	ζ	$I(10^{-6})$
10	261.33	233.33	11.31	6.09 10^{-4}	0.375
			$\ell=1$		
freq. number	ν	σ^2	$\nu/\Delta\nu$	ζ	I (10^{-6})
#1	249.62	212.88	10.80	0.422	0.867
#2	252.93	218.58	10.94	0.799	2.333
#3	258.52	228.34	11.18	0.937	7.512
#4	264.70	239.37	11.45	0.928	5.759
#5	270.52	250.02	11.70	0.657	0.922
#6	273.65	255.84	11.84	0.498	0.578

Table 3. Normalized radius of the turning points for selected modes for model M1 frequencies: the g-cavity is delimitated by $[x_1,x_2]$ and the p cavities by $[x_3,x_4]$. In the other regions the modes are evanescent. We find $x_1=1.3\ 10^{-4}$ and $x_4=0.9999$ for all listed modes

	x_2	x_3
#1	0.0732	0.119
#2	0.0725	0.118
#3	0.0715	0.116
#4	0.0705	0.113
#5	0.0693	0.111
#6	0.0689	0.110

4.2.1. Mode inertia I and rotational splittings

The rotational splittings for ν_1 to ν_6 are displayed in Fig.7. The relative contributions I_1/I related to z_1^2, and I_2/I related to z_2^2, defined as

$$\frac{I_1}{I}=\frac{1}{I}\int_0^1 z_1^2\,\frac{{\rm d}x}{x}\quad;\quad\frac{I_2}{I}=\frac{1}{I}\int_0^1 z_2^2\,\frac{{\rm d}x}{x}\qquad(14)$$

are displayed in Fig.7.

The contribution of the z_1z_2 terms to the rotational splittings (Eq.11) is negligible in front of z_1^2 in the envelope and in front of z_2^2 in the core. Thus, the following conclusions apply for both the mode inertia and the rotational splittings.

The I_1 contribution coincides to a good approximation with the envelope contribution $I_{\rm env}$, while the I_2 contribution coincides to a good approximation with the core contribution. The core contribution to inertia, $I_{\rm core}$, and the rotational kernel, $K_{\Omega,core}=\int_{core}\Omega(x)\ K(x)\ {\rm d}x$, are computed between the lower and upper turning points of the g cavity for each mode. The dense core contributes heavily to the total mode inertia I and rotational splittings. The values of the ratio $\zeta=I_{\rm core}/I$ are given in Table 2.

– The modes with frequencies ν_3 and ν_4 are g-m modes. For these modes, the contribution of the horizontal displacement z_2 (essentially in the core) dominates their inertia ($I_2/I\sim I_{\rm core}/I\approx 1$) while the contribution due to the radial displacement z_1 (largest in the envelope), I_1/I, is negligible.
The envelope above the core where the mode is either evanescent or of acoustic type contributes for almost

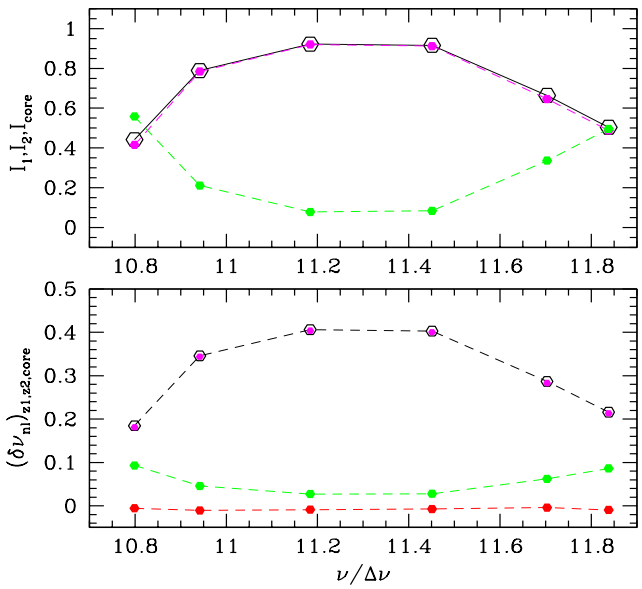

Fig. 7. *Top:* relative inertia contributions I_1/I (green dots connected dashed line dots correspond to modes) and I_2/I (Eq.14) (black), relative contribution $\zeta = I_{\rm core}/I$ (magenta dashed line, hexagons correspond to modes). *Bottom:* contribution to the rotational splittings for model M1 due to z_1^2 only (green dashed line dots correspond to modes), contribution due to z_2^2 only (black dashed lines and hexagons), contribution due to $z_1 z_2$ only (red-dashed line, dots correspond to modes); contribution to $\delta\nu_{nl}$ due to the core only (magenta filled hexagons)

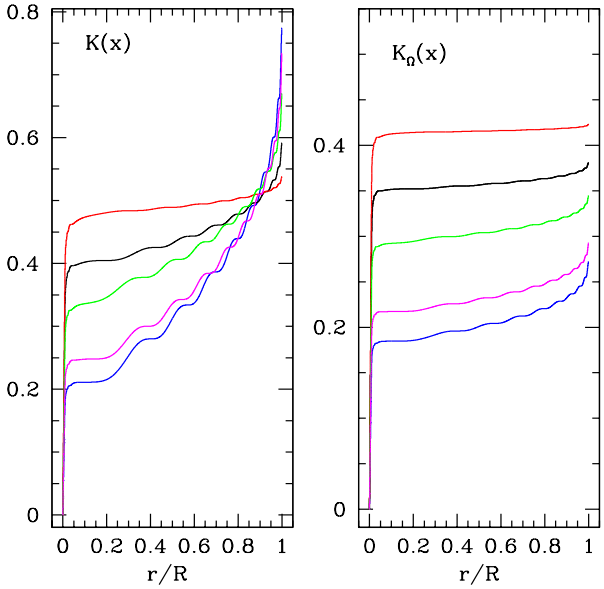

Fig. 8. Integrated kernels $\int_0^x K(x')\,{\rm d}x'$ (left panel) and $\int_0^x \Omega(x)\ K(x')\,{\rm d}x'$ (right panel) (with $K(x)$ given by Eq. 12) as a function of $x = r/R$ for some modes of the selected pattern for model M1. The lines correspond to mode # 1 (blue); # 2 (black); # 4(red); # 5 (green) and # 6 (magenta) of Tab.2 respectively.

nothing to the total mode inertia $I_{\rm env}/I = 1 - \zeta \ll \zeta$ for such modes. The contribution of the envelope to $\delta\nu$ is negligible because the rotation is quite small there.

– The other modes are p-m modes. The envelope above the core where the mode is either evanescent or of acoustic type contributes for half for these modes ($I_1 \sim I_2 \sim I/2$). They share their inertia almost equally in the core and in the envelope with an almost equal contribution of the horizontal and radial displacements.

4.2.2. Integrated kernels

The modes are trapped in the same g cavity, thus they probe the same inner part of the rotational profile of the model. This can be seen with the behavior of the integrated rotational kernels that are shown in Fig. 8 (left panel). For all modes of the pattern, the integrated rotational kernels increase rapidly from the center.

– For the g-m modes, the integrated kernels saturate quite rapidly to the maximum value, indicating that the envelope does not significantly contribute. This is the case for ν_4 in our studied pattern. Note that the saturated value is obtained long before the upper turning point of the g cavity is reached. This is due to the fact that the amplitudes of the displacement become rapidly small in the upper part of the g-cavity.

– The p-m modes such as ν_1 and ν_6 have their integrated kernels that saturate less rapidly and to a much smaller value than the g-m modes. The corresponding integrated contributions to the splittings are shown in Fig. 7 and 8 (right panel). As they include the rotation profile, they increase faster than the integrated rotational kernel.

5. Seismic constraint on rotation

To have more physical insight into the information carried by rotational splittings it is worthwhile to emphasize their dependences. To this end, we decompose the rotational splittings into two contributions. Given that the inner (radiative) and outer (convective) cavities have well distinct properties, we write:

$$\delta\nu = \beta_{\rm core} \left\langle \frac{\Omega}{2\pi} \right\rangle_{\rm core} + \beta_{\rm env} \left\langle \frac{\Omega}{2\pi} \right\rangle_{\rm env} , \qquad (15)$$

where

$$\beta_{\rm core} \equiv \int_0^{x_{\rm core}} K(x)\ \ {\rm d}x\,, \qquad (16)$$

$$\beta_{\rm env} \equiv \int_{x_{\rm core}}^{1} K(x)\ \ {\rm d}x = \beta - \beta_{\rm core}\,, \qquad (17)$$

and

$$\langle\Omega\rangle_{\rm core} \equiv \frac{\int_0^{x_{\rm core}} \Omega(x')\ K(x')\ \ {\rm d}x'}{\int_0^{x_{\rm core}} K(x')\ \ {\rm d}x'}\,, \qquad (18)$$

$$\langle\Omega\rangle_{\rm env} \equiv \frac{\int_{x_{\rm core}}^{1} \Omega(x')\ K(x')\ \mathrm{d}x'}{\int_{x_{core}}^{1} K(x')\ \mathrm{d}x'}\,, \tag{19}$$

where $K(x)$ is defined in Eq. (12) and $\langle\Omega\rangle_{\rm core}$ is the angular rotation velocity averaged over the central layers enclosed within a radius $x_{\rm core} = r_{\rm core}/R$ corresponding to the g resonant cavity. The radius $x_{\rm core}$ is taken as the radius of the upper turning point of the g cavity x_2 (see Table 3 for one pattern). $\langle\Omega\rangle_{\rm env}$ is defined as the angular rotation velocity averaged over the layers above $x_{\rm core}$.

For the modes we consider in this paper, the evanescent regions above the g resonant cavity and above the p cavity are narrow. Then, the envelope essentially corresponds to the p resonant cavity. The boundary radii are then taken as x_3 and x_4 (see Table 3). Strictly speaking, the above quantities depend on the mode (actually on its frequency) because they are defined in the propagative cavities characteristics of each mode. However, because of the sharp decrease of the Brunt-Väisälä frequency at the edge of the H shell burning region, the upper turning point of the g cavity is roughly the same for all modes (see Table 3). The modes have a significant amplitude in the g cavity in a region that is quite narrower than the extent of the g cavity and that is independent of the mode (in the frequency regime we consider). This can be seen in Fig. A.1 where the horizontal and radial displacement eigenfunctions are shown for two typical modes of the studied pattern with frequencies listed in Table 2. We can then consider that $x_{\rm core}$ and the quantity $\langle\Omega\rangle_{\rm core}$ are nearly the same for all considered modes.

The radius of the lower turning-point, x_3, for the p-cavity of p-m $\ell = 1$ modes decreases slightly with increasing frequency of the mode while the upper turning point remains approximately the same (see Table. 3). Thus, mode inertia remains dependent on the mode. On the other hand, the mean envelope rotation is nearly that given by the uniform rotation of the convective zones and remains the same for all modes.

$$\langle\Omega\rangle_{\rm env} \approx \Omega_{\rm CZ}\,. \tag{20}$$

In Fig. 4, the rotational splittings obtained with two approximations for $\langle\Omega\rangle_{\rm core}$ are compared with the exact calculation Eq. (11). The core contribution to the rotational splittings $\langle\Omega\rangle_{\rm core}\beta_{\rm core}$ (Eqs. (15) and (18)) is displayed with the magenta dots connected with the magenta dotted line. The blue crosses dotted line represents the core contribution to the rotational splittings (Eq. (15)) with $\langle\Omega\rangle_{\rm core}$ computed with only the horizontal eigenfunction z_2. The two variations (magenta dots and blue crosses) cannot be distinguished. The blue dotted line represents the contribution from the envelope to the rotational splittings $\langle\Omega\rangle_{\rm env}\ (\beta - \beta_{\rm core})$. This contribution is much smaller for model M2 than for model M1.

For the g-m modes (i.e. for $\zeta \sim 1$), $\beta_{\rm core} \approx 1/2$. The maximum rotational splitting is then given by

$$\delta\nu_{\rm max} = \frac{1}{2}\ \left\langle \frac{\Omega}{2\pi} \right\rangle_{\rm core}\,. \tag{21}$$

The maximum values of the computed rotational splittings, $\delta\nu_{\rm max}$, reach 0.44 and 0.430 μHz for M1 and M2 models respectively. These values give rise to a mean core rotation $\langle\Omega/2\pi\rangle_{\rm core} = 0.88\ \mu$Hz and 0.86 μHz, which are close to but smaller than the central rotation for models M1 and M2 respectively (resp. 0.97 and 0.95 μHz). This is explained by the fact that the rotation decreases sharply in the central regions of our models and that the major contribution to the rotational splitting is slightly shifted off the center as are the maximum amplitudes of the horizontal displacement eigenfunctions (Fig. A.1) and the rotational kernels.

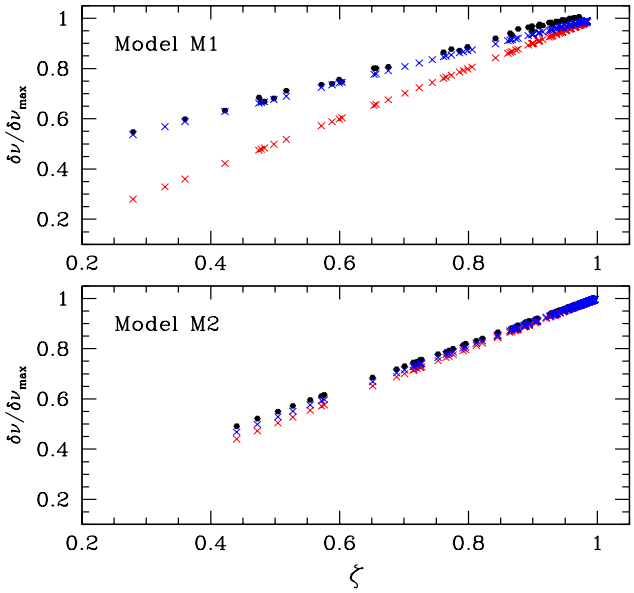

Fig. 9. The rotational splitting normalized to its maximum value as a function of ζ (black dots) for model M1 (top) and model M2 (bottom). The red crosses represent the approximation $\delta\nu/\delta\nu_{\rm max} = \zeta$ as a function of ζ. The blue crosses represent the approximation $\delta\nu/\delta\nu_{\rm max} = \zeta(1-2\mathcal{R})+2\mathcal{R}$ as a function of ζ with $R = 0.1785$ and using numerical values of ζ.

Moreover, for $\ell = 1$ modes, one obtains $\beta_{\rm core} \simeq \zeta/2$, $\beta = 1-\zeta/2$, and $\beta_{\rm env} = 1-\zeta$, to a very good approximation (Eq. (A.5) in Appendix A.2). Then the linear rotational splitting Eq. (15) is easily rewritten as

$$\frac{\delta\nu}{\delta\nu_{\rm max}} = \zeta\ (1-2\mathcal{R}) + 2\mathcal{R}\,, \tag{22}$$

where we have defined the ratio

$$\mathcal{R} \equiv \frac{\langle\Omega\rangle_{\rm env}}{\langle\Omega\rangle_{\rm core}}\,. \tag{23}$$

The splittings linearly increase with ζ. This linear dependence is verified using the numerical frequencies computed for model M1 and M2 and is shown in Fig. 9.

We stress that for model M2 the ratio $\mathcal{R}$ imposed by our choice of rotation profile is quite small and the approximation

$$\delta\nu \approx \frac{1}{2}\left\langle \frac{\Omega}{2\pi} \right\rangle_{\rm core}\ \zeta \tag{24}$$

is in agreement with the numerical splitting values.

We find that the rotational splittings of p-m modes as well as g-m modes are dominated by the central layers for model M2. For the most g-dominated modes, $\zeta \sim 1$ and the rotational splittings in that case directly give half the mean core rotation.

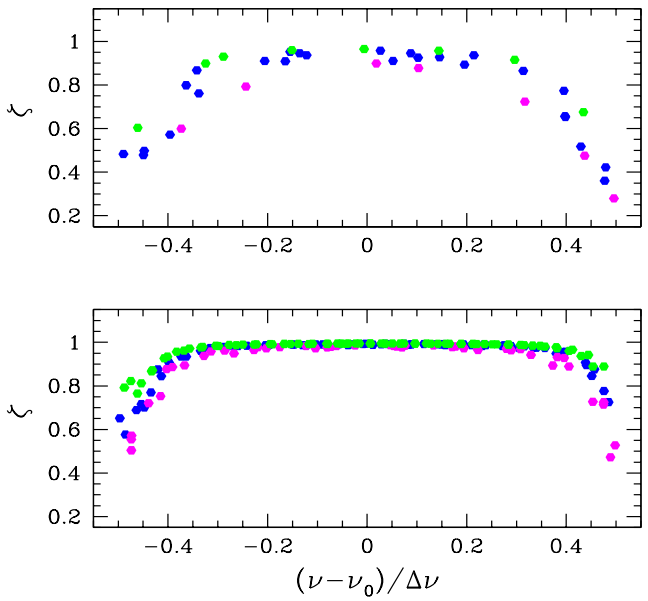

Fig. 10. $\zeta = I_{\rm core}/I$ as a function $(\nu - \nu_0)/\Delta\nu$ for all $l = 1$ modes for model M1 (top panel) and for model M2 (bottom panel). ν_0 is the frequency of the closest radial mode for the l=1 mode with frequency ν. For model M1, blue dots correspond to modes with $9 < \nu/\Delta\nu < 15$; magenta dots to modes with $\nu/\Delta\nu > 15$ and green dots to modes with $\nu/\Delta\nu < 9$). For model M2, blue dots correspond to modes with $8 < \nu/\Delta\nu < 12$; magenta dots to modes with $\nu/\Delta\nu > 12$ and green dots to modes with $\nu/\Delta\nu < 8$).

This is not true for less-evolved models such as model M1 for which the approximation Eq. (24) is not sufficient (Fig. 9). The contribution from the envelope layers is not negligible for the rotation profiles we have assumed and the surface rotation must be taken into account as in Eq. (22). This is explained by the fact that the p cavity extends quite deep downward inside the model where the rotation already shows a sharp gradient toward the center.

The interest of Eq. (22) is that ζ as well as $\delta\nu$ and $\delta\nu_{max}$ can be obtained from observations. Mosser et al. (2012b,a) have shown that it is possible to identify the $m = 0$ modes and their nature (p- or g-dominated mixed). We show here that it is also possible to attribute them a ζ value from the observations. We use as proxy for the measure of the g nature of the mixed mode the distance of the $\ell = 1$ mode frequency from that of its companion radial mode: $\nu - \nu_0$.

Figure 10 shows the ζ values for $\ell = 1$ modes as a function of $\nu - \nu_0$ for models M1 and M2 where ν_0 is the frequency of the radial mode closest to ν. The ζ values all follow the same curve. Due to this monotonic dependence, it is possible to estimate the value of ζ from observations (*i.e.*, from the knowledge of $\nu - \nu_0$). The dispersion of the ζ values about the mean curve in Fig. 10 introduces uncertainties on the induced ζ value. This nevertheless offers a mean to derive not only $\delta\nu_{\rm max}$ – hence the mean core rotation – but also the ratio $\mathcal{R}$, hence a measure of the mean rotation gradient from observations.

6. Physical interpretation of the observed splittings

In this section, we show that rotational splittings can be expressed as a function of observables. Indeed, this will further permit us to derive physical properties related to rotation by using observations only (see Sect. 7).

We interpret physically the two components of the rotational splitting $\langle\Omega\rangle_{\rm core}$ and $\langle\Omega\rangle_{\rm env}$ as the rotation angular velocities averaged over the time spent in the g and p cavities, respectively. We checked numerically with our stellar models and numerical frequencies and eigenfunctions that $\langle\Omega\rangle_{\rm core}$ and $\langle\Omega\rangle_{\rm env}$ are well approximated by mean rotations defined as

$$\bar{\Omega} = \frac{1}{\tau} \int \Omega(x)\ {\rm d}\tau. \tag{25}$$

The time spent by the mode is approximately given by

$$\tau \approx \frac{2}{\sigma} \int k_{\rm r}\ {\rm d}x\,, \tag{26}$$

(Unno et al. 1989, and references therein) where σ is the normalized frequency of the mode. The radial wave number of the wave normalized to the stellar radius, $k_{\rm r}$, is given, in a local asymptotic analysis, by

$$k_{\rm r}^2 = \frac{1}{\sigma^2}\frac{1}{c_s^2}\Big(N^2 - \sigma^2\Big)\Big(S_\ell^2 - \sigma^2\Big)\,, \tag{27}$$

(Osaki 1975; Unno et al. 1989) where N^2 and S_l^2 are the normalized squared Brunt-Väisälä and Lamb frequencies, respectively. As will be seen below, the level of approximation is sufficient for our purpose.

In the g cavity, $\sigma^2 \ll S_\ell^2$, therefore

$$k_r \approx \frac{\sqrt{\Lambda}}{\sigma x}\ (N^2 - \sigma^2)^{1/2}\,, \tag{28}$$

then the time spent in the resonant g cavity becomes

$$\tau_g = 2\ \frac{\sqrt{\Lambda}}{\sigma^2} \int_{\rm core} (N^2 - \sigma^2)^{1/2}\ \frac{{\rm d}x}{x}\,. \tag{29}$$

Note that this provides the number of nodes in the g cavity as n_g that is defined as $2\pi n_{\rm g}/\sigma = \tau_{\rm g}$.

Similarly, in the acoustic cavity in the envelope where $\sigma^2 \gg N^2, S_l^2$, one can write

$$\tau_p = 2 \int_{\rm env} \frac{k_r}{\sigma}\ {\rm d}x \approx 2 \int_{\rm env} \frac{{\rm d}x}{c_s}\,. \tag{30}$$

Note that the time τ_p and τ_g are defined in units of the dynamical time $t_{\rm dyn} = (GM/R^3)^{-1/2}$.

The expressions for the mean core (resp. envelope) rotation become

$$\bar{\Omega}_{core} = \frac{1}{\tau_g} \int_{\rm core} \Omega(x)\ \frac{N}{x}{\rm d}x\,, \tag{31}$$

$$\bar{\Omega}_{\rm env} = \frac{1}{\tau_p} \int_{\rm env} \Omega(x)\ \frac{{\rm d}x}{c_s}\,. \tag{32}$$

The theoretical values of $\bar{\Omega}_{\rm env}$ and $\bar{\Omega}_{\rm core}$, Eqs. (31) and (32), are computed for both equilibrium models M1 and M2. We find $\bar{\Omega}_{\rm core}/2\pi = 0.88$ μHz, $\bar{\Omega}_{\rm env}/2\pi = 0.157$ μHz then $\delta\nu_{\rm max,th} = 0.44$ μHz, $\mathcal{R} = 0.178$ for model M1 and $\bar{\Omega}_{\rm core}/2\pi = 0.856$ μHz, $\bar{\Omega}_{\rm env}/2\pi = 0.042$ μHz, $\delta\nu_{\rm max,th} =$

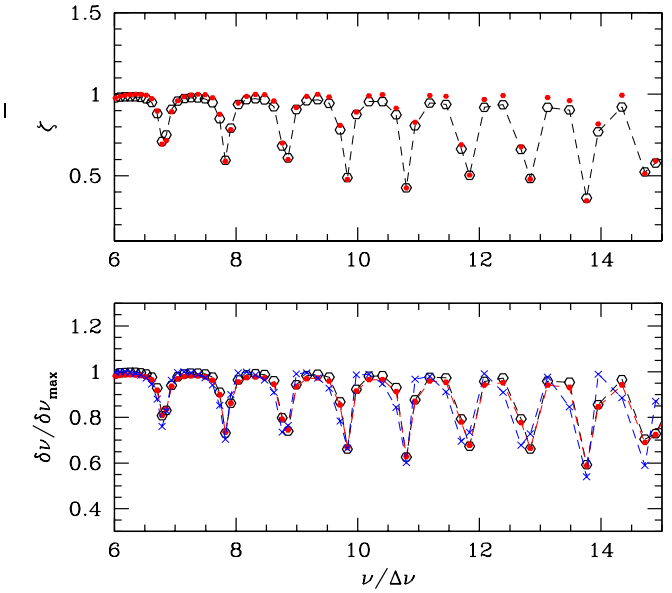

Fig. 11. *Top:* ζ as a function of $\nu/\Delta\nu$. Black open symbols: numerical results (Eq.10). Red dots: ζ approximated by (Eq.33) with $\chi = 2.5\ y\cos(\pi/(\Delta\Pi\nu))$ and $y = \nu/\Delta\nu$. *Bottom:* $\delta\nu/\delta\nu_{\rm max}$ as a function of $\nu/\Delta\nu$. Black dots: numerical values (Eq.11). Red dots: approximate expression for $\delta\nu/\delta\nu_{\rm max}$ (Eq.22) with $\mathcal{R} = 0.1785$ and ζ given by its numerical values. Blue crosses: $\delta\nu/\delta\nu_{\rm max}$ given by Eq.37 with $\mathcal{R} = 0.1785$ and χ given by Eq.34.

0.428 μHz, $\mathcal{R} = 0.05$ for model M2 where the subscript th stands for theoretical.

We then computed the rotational splittings from the approximate expression Eq. (22) using these figures with ζ computed with the associated eigenfunctions (Eq.10). As a result, the theoretical dependence given by Eq. (22) perfectly matches the numerical curve $\delta\nu/\delta\nu_{\rm max}$ and $\bar{\Omega}_{\rm core} \sim \langle\Omega\rangle_{\rm core}$, $\bar{\Omega}_{\rm env} \sim \langle\Omega\rangle_{\rm env}$. This can be seen in Fig. 11 for model M1 where one compares the behavior of the numerical splittings $\delta\nu/\delta\nu_{\rm max}$ with $\nu/\Delta\nu$ to the splitting values obtained by using Eq. (22).

One can go to a further level of approximation by deriving an approximate expression for the mode inertia. Appendix A.3 shows that one can derive an approximate expression for ζ as

$$\zeta \approx \frac{1}{1+\alpha_0\ \chi^2}\,, \tag{33}$$

where

$$\chi \approx 2\ \frac{\nu}{\Delta\nu}\ \cos\left(\frac{\pi}{\Delta\Pi\ \nu}\right) = 2\ y\ \cos\left(\frac{\pi}{\alpha_0\ y}\right)\,. \tag{34}$$

For convenience we have defined $y = \nu/\Delta\nu$ and a dimensionless constant α_0 as

$$\alpha_0 = \Delta\nu\ \Delta\Pi\,, \tag{35}$$

with $\Delta\Pi$ is the period spacing for g-m modes

$$\Delta\Pi = \frac{2\pi^2}{\sqrt{\Lambda}}\ \left(\int_{\rm core}\ \frac{(N^2-\sigma^2)^{1/2}}{x}\ {\rm d}x\right)^{-1}\,. \tag{36}$$

Table 4. Typical values for the quantity $4\alpha_0\ y_{\rm n_0}^2$ (Eq.(39)) for stars on the RGB and in the clump. $\Delta\nu$ and ν_{max} are given in μHz and $\Delta\Pi$ in seconds. The values in parenthesis corresponds to y_{n_0} evaluated at $\nu_{\rm max} \pm 3\Delta\nu$.

$\Delta\nu$	$\nu_{\rm max}$	$\Delta\Pi$	$4\alpha_0\ y_{\rm n_0}^2$	stage
40	500	120	3.0 (1.73, 5.23)	bottom RGB
10	120	80	0.46 (0.26, 0.82)	mid RGB
4	35	60	0 .074 (0.03, 0.16)	top RGB
4	35	300	0.43 (0.01, 0.09)	clump

For models M1 and M2, we respectively have $\alpha_0 = 2.2\ 10^{-3}$ and $\alpha_0 = 6.0\ 10^{-4}$.

The behavior of the ratio ζ as a function of $\nu/\mathbf{\Delta}\nu$ is computed with Eq. (33) and Eq. (34) and is compared to that of the numerical one in Fig. 11 (top). The cosine term gives rise to the oscillation of ζ while the decrease of the minimum values of ζ with frequency is driven by the ratio τ_p/τ_g. ζ is computed using Eq. (33) and Eq. (34) where the factor 2 is replaced by a factor 2.5 which fits better the numerical results. This difference is explained by the fact that we took the factor f (Appendix A.3) equal to unity while it is in reality smaller. For model M1 the difference between the large separation $\Delta\nu$ and the equivalent quantity computed over the p resonant cavity is of the order of $f = 0.8$. This increases the constant in χ from 2 to 2.24, closer to the the adopted 2.5 value. As mentionned also in Appendix A.3, the amplitude ratio Eq. (A.20) is further increased if one takes into account the effect of the evanescent zone between the outer p and inner g resonant cavities of modes. As a consequence, this leads to an increase of the χ term contribution. Actually, some departure from asymptotic is expected for the p part of red giants modes. It is then striking that the numerical results agree that well with Eq. (33).

An expression for the normalized rotational splitting as a function of the observable $y \equiv \nu/\Delta\nu$ is then obtained by combining Eq. (22) and Eq. (33) so that

$$\frac{\delta\nu}{\delta\nu_{\rm max}} \approx \frac{1-2\mathcal{R}}{1+\alpha_0\ \chi^2} + 2\mathcal{R}\,, \tag{37}$$

with χ given by Eq. (34).

The rotational splittings computed with Eq. (34) and Eq. (37) are compared with the numerical values for model M1 in Fig. 11. The behavior of both theoretical and numerical quantities agree quite well. An illustration is provided in Sect. 7 with the red giant star KIC 5356201 (Beck et al. 2012) for which such a procedure has been used.

The ratio $\delta\nu/\delta\nu_{\rm max}$ as a function of $(\nu-\nu_0)/\delta\nu$ is nearly independent of rotation, in particular when $\mathcal{R} \ll 1$. Maxima of the ζ oscillation are obtained for $\cos\big(\pi/(\alpha_0\ y)\big) = 0$, then $\zeta_{\rm max} = 1$. Minima are defined for $\cos\big(\pi/(\alpha_0 y_{\rm n_0})\big) = \pm 1$, *i.e.*, $\alpha_0 y_{\rm n_0} = 1/n_0$ (for any integer n_0) then

$$\zeta_{\rm min} \approx \left(1+4\ \alpha_0\ y_{\rm n_0}^2\right)^{-1}\,. \tag{38}$$

Accordingly, the contrast η defined as the ratio of minimum to maximum splittings is obtained from Eq. (37) using Eq. (38) and Eq. (A.23) as

$$\eta \equiv \frac{\delta\nu_{\rm min}}{\delta\nu_{\rm max}} = \frac{1-2\mathcal{R}}{1+4\ \alpha_0\ y_{\rm n_0}^2} + 2\mathcal{R}\,. \tag{39}$$

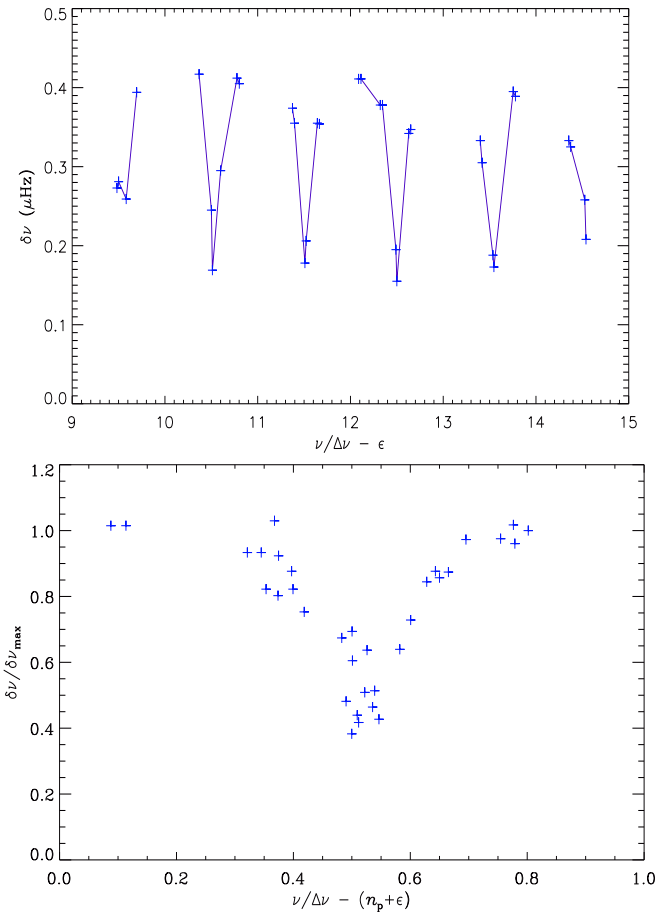

Fig. 12. *Top:* Observed rotational splittings as a function of $\nu/\Delta\nu$ for the Kepler star KIC 5356201 (Beck et al. 2012). For this star, the mean large separation is $\Delta\nu = 15.92\mu$ Hz while the mean g -mode spaging is $\Delta\Pi = 86.11$s and the maximum rotational splittings is $\delta\nu_{\rm max} = 0.405$nHz. *Bottom:* Rotational splittings normalized to $\delta\nu_{\rm max}$ are folded with $(\nu - \nu_0)/\Delta\nu$.

As $4\alpha_0\ y_{\rm n_0}^2$ decreases with increasing integer n_0, the contrast $\delta\nu_{\rm min}/\delta\nu_{\rm max}$ increases with frequency for a given rotation profile. This can be seen quite clearly for model M2 in Fig. 5 for instance.

Typical values of the quantity $4\alpha_0\ y_{\rm n_0}^2$ for different types of observed red giants are listed in Tab. 4, according to the analysis done by Mosser et al. (2012b). For simplicity, $y_{\rm n_0}$ is evaluated at $\nu = \nu_{\rm max}$. The first two lines are given for red giants corresponding well to models M1 and M2 respectively discussed in the previous sections. More generally, this quantity decreases from about 4 at the bottom of the RGB down to 0.06 for red giants stars located on the highest part of the RGB for which stochastically oscillations are detected. It amounts to roughly 0.4 for the clump stars. Note that for the most evolved red giant stars, $4\alpha_0\ y_{\rm n_0}^2$ is quite small. In that case, the contrast η varies as

$$\eta \equiv \frac{\delta\nu_{\rm min}}{\delta\nu_{\rm max}} \sim 1 - 4\ \alpha_0\ y_{\rm n_0}^2\ (1 - 2\mathcal{R})\,. \qquad (40)$$

and the influence of the rotation on this contrast throughout $\mathcal{R}$ can become negligible.

7. The illustrative case of the red giant KIC 5356201

Differential rotation of the red giant KIC 5356201 observed by *Kepler* has been analyzed by Beck et al. (2012). As the inclination of the star has an intermediate value, the three components of the dipole mixed-mode multiplets are clearly visible, that allows a precise determination of the rotational splittings. With $\nu_{\rm max} = 209.7 \pm 0.7\mu$Hz, $\Delta\nu = 15.92 \pm 0.02\,\mu$Hz and a period spacing $\Delta\Pi = 86.2 \pm 0.03$ s, determined according to the method presented in Mosser et al. (2012b), the star lies at the bottom of the RGB, with a seismically inferred radius of about 4.5 $R_\odot$. The minimum rotational splitting given by Beck et al. (2012) is 0.154 $\pm$0.003 μHz; the authors also mention that the average contrast between the maximum and minimum value of the splittings is 1.7; the maximum value inferred by Mosser et al. (2012b) is 0.405$\pm$0.010 μHz. With such global seismic parameters, one infers that this star is slightly more evolved than model M1 but can be approximately represented by this model.

The observational rotational splittings are displayed as a function of $\nu/\Delta\nu$ (ν is the frequency of the centroid mode of each identified multiplet) in Fig. 12 (top). The folded splittings are shown in Fig. 12 (bottom). The global behavior of the curve shows the same characteristics as the theoretical equivalent in Fig. 6 for model M1. Only the value of the minimum at $(\nu - \nu_0)/\Delta\nu$ is smaller than 0.4 (Fig. 12) for the observations compared with 0.59 for model M1 (Fig.6). The difference is due to different values of the parameters α_0 ($\alpha_0 = 1.37\ 10^{-3}$ for the Kepler star).

Using the observed values for $\nu_{\rm max}, \Delta\nu$ and $\mathbf{\Delta}\Pi$ for the star KIC 5356201, we find $\eta = 0.49$ (Eq. (39)) when evaluated for the mode with frequency $\nu/\Delta\nu = 13.7 (\sim \nu_{\rm max}/\Delta\nu)$. This is close to the observed contrast $\delta\nu/\delta\nu_{max} = 0.43$ evaluated for the same mode. Note that if one corrects η with the factor f mentioned above, taking a typical $f = 0.8$ as for model M1, one obtains $\eta = 0.45$ even closer to the observed value.

In Fig. 13 (top), the observed rotational splittings normalized to their maximum value $\delta\nu_{\rm max}$ are plotted as a function of ζ obtained using Eqs. (33) and (34). The linear dependence of the observed rotational splittings with ζ is clear. One single parameter, $2\mathcal{R}$, enters the expression for $\delta\nu/\delta\nu_{max}$ (Eq.22) and can then be estimated to range between 0. and 0.1 from Fig. 13 (top). This indicates that for this star the ratio between the average core rotation and that of the convective envelope is larger than 20.

We next compare the theoretical rotational splittings computed using Eqs. (34) and (37) with the observed rotational splittings in Fig. 13 (bottom). The agreement is quite acceptable and validates our theoretical derivations of Sect. 6.

8. Conclusion

We have investigated the properties of the rotational splittings of dipole ($\ell = 1$) modes of red giant models. The rotational splittings are computed with a first-order perturbation method because we focused on slowly-rotating red giant stars. We considered two models in two different H shell-burning evolutionary stages. We find that such modes are either g-m modes (inertia and rotational splittings are fully dominated by the core properties) or p-m modes (inertia is almost equally shared between the core and the en-

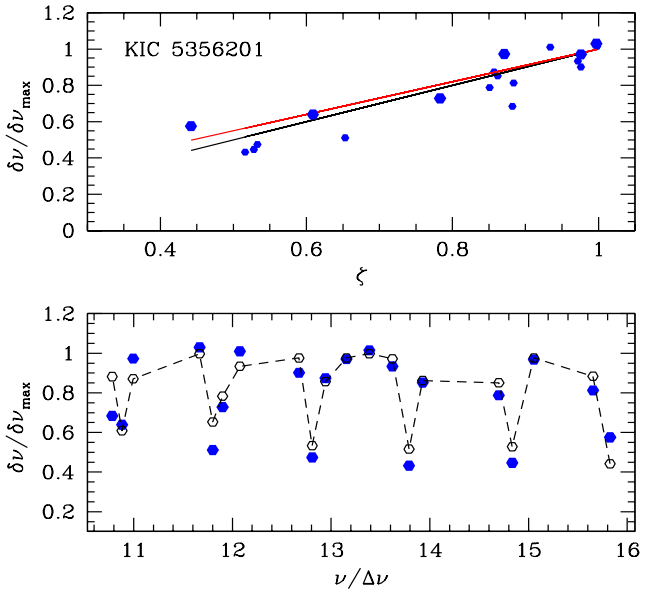

Fig. 13. *Top:* Observed rotational splittings as a function of ζ computed with Eq.33 and Eq.34 for the Kepler star KIC 5358201 (blue dots). The solid curves are $\zeta(1-2\mathcal{R})+2\mathcal{R}$ with $\mathcal{R}=0$ (black) and $2\mathcal{R}=0.1$ (red). *Bottom:* Observed rotational splittings (blue filled dots)as a function of $\nu/\Delta\nu$. Theoretical rotational splittings computed according to Eq.37 and Eq.34 (black open dots connected with a dashed line) with $\mathcal{R}=0$.

velope). For g-m modes, the rotational splittings are fully dominated by the average core rotation. As the time spent by all considered g-m modes in the core is roughly the same, the resulting mean core rotation corresponds to the rotation in the central layers weighted by the time spent by the modes in the core. For a radiative core, if the rotation is decreasing sharply from the center, the mean core rotation is a lower limit of the central rotation. For p-m modes, the rotational splittings remain dominated by the core rotation but the contribution of the envelope is no longer negligible.

We find that the rotational splittings normalized to their maximum value linearly depend on the core contribution of mode inertia. The slope provides the ratio of the average envelope rotation to the core one ($\mathcal{R}$). Mode inertia is univocally related to the frequency difference between observed $\ell=1$ modes and the frequency of the closest radial mode. As this last quantity is measurable, one can use the simple relation between the core inertia and this frequency difference to determine the core inertia. This knowledge together with a measure of the rotational splitting then provides a measure of $\mathcal{R}$.

As a step further in the modeling, we used asymptotic properties to show that the core contribution to mode inertia relative to the total mode inertia depends on the frequency normalized to the large separation through a Lorentzian. This provides a theoretical support for the use of a Lorentzian profile for measuring the observed splittings for red giant stars (Mosser et al. 2012a). This also led us to find that the behavior of the rotational splittings of $\ell=1$ modes with the frequency for slowly rotating core red giant stars depends on three parameters only. One is the large separation $\Delta\nu$, the second is the g-mode period spacing $\Delta\Pi$, both can be determined observationally and can therefore provide again a measure of the third one, $\mathcal{R}$.

The contrast between the minimum ($\delta\nu_{\rm min}$) and maximum ($\delta\nu_{\rm max}$) values of the splittings can be evaluated at the frequency of maximum power. It depends only on the above 3 parameters. For a core rotating much faster than the envelope (negligible $\mathcal{R}$), we obtain a relation between ($\delta\nu_{\rm min}$), ($\delta\nu_{\rm max}$), $\Delta\nu$ and $\Delta\Pi$. This can provide ($\delta\nu_{\rm max}$) (hence the average core rotation) in case when the g-m modes have too small amplitudes to be detected and only ($\delta\nu_{\rm min}$) is available.

Based on the above theoretical developments, we find that the Kepler red giant star KIC 53656201 observed by Kepler (Beck et al. 2012) rotates with a rotation in the convective envelope $\Omega_{CZ} < 0.05\ \langle\Omega\rangle_{\rm core} \leq \Omega(r=0)$ so that the core is rotating more than 20 times faster than the envelope.

The present understanding of the properties of rotational splittings is a contribution to the effort to decipher the effect of slow rotation on red giant star frequency spectra and establish seismic diagnostics on rotation and transport of angular momentum. For more rapidly rotating red giant stars, non-perturbative methods must be used. This will be the subject of the third paper of this series.

Acknowledgements. JPM acknowledges financial support through a 3 year CDD contract with CNES. R-M.O. is indebted to the "Fédération Wallonie- Bruxelles - Fonds Spéciaux pour la Recherche / Crédit de démarrage - Université de Liège" for financial support. The authors also acknowledge financial support from the French National Research Agency (ANR) for the project ANR-07-BLAN-0226 SIROCO (SeIsmology, ROtation and COnvection with the CoRoT satellite). We also thank the anonymous referee for a careful reading of the manuscript and useful suggestions.

References

Baglin, A., Auvergne, M., Boisnard, L., et al. 2006, in 36th COSPAR Scientific Assembly, Vol. 36, 3749
Ballot, J., Lignières, F., Prat, V., Reese, D. R., & Rieutord, M. 2011, ArXiv e-prints
Ballot, J., Lignières, F., Reese, D. R., & Rieutord, M. 2010, A&A, 518, A30
Beck, P. G., Montalban, J., Kallinger, T., et al. 2012, Nature, 481, 55
Bedding, T. R. & Kjeldsen, H. 2003, PASA, 20, 203
Bedding, T. R., Mosser, B., Huber, D., et al. 2011, Nature, 471, 608
Belkacem, K., Goupil, M. J., Dupret, M. A., et al. 2011, A&A, 530, A142
Borucki, W. J., Koch, D., Basri, G., et al. 2010, Science, 327, 977
Brown, T. M., Gilliland, R. L., Noyes, R. W., & Ramsey, L. W. 1991, ApJ, 368, 599
Christensen-Dalsgaard, J. 2008, Ap&SS, 316, 113
Christensen-Dalsgaard, J. & Berthomieu, G. 1991, Theory of solar oscillations, ed. A. N. Cox, W. C. Livingston, & M. S. Matthews, 401–478
De Ridder, J., Barban, C., Baudin, F., et al. 2009, Nature, 459, 398
Deheuvels, S., García, R. A., Chaplin, W. J., et al. 2012, ApJ, 756, 19
Dupret, M.-A., Belkacem, K., Samadi, R., et al. 2009, A&A, 506, 57
Dziembowski, W. 1977, Acta Astron., 27, 95
Dziembowski, W. A. 1971, Acta Astron., 21, 289
Dziembowski, W. A., Gough, D. O., Houdek, G., & Sienkiewicz, R. 2001, MNRAS, 328, 601
Eggenberger, P., Montalbán, J., & Miglio, A. 2012, A&A, 544, L4
Hekker, S., Kallinger, T., Baudin, F., et al. 2009, A&A, 506, 465
Kjeldsen, H. & Bedding, T. R. 1995, A&A, 293, 87
Ledoux, P. 1951, ApJ, 114, 373
Lignières, F. 2011, in Lecture Notes in Physics, Berlin Springer Verlag, Vol. 832, Lecture Notes in Physics, Berlin Springer Verlag, ed. J.-P. Rozelot & C. Neiner, 259

Marques, J. P., Goupil, M. J., Lebreton, Y., et al. 2012, A&A(submitted)
Meynet, G., Ekstrom, S., Maeder, A., et al. 2012, Lectures Notes in Physics (in press)
Montalbán, J., Miglio, A., Noels, A., Scuflaire, R., & Ventura, P. 2010, ApJ, 721, L182
Mosser, B., Barban, C., Montalbán, J., et al. 2011a, A&A, 532, A86
Mosser, B., Belkacem, K., Goupil, M. J., et al. 2011b, A&A, 525, L9
Mosser, B., Belkacem, K., Goupil, M.-J., et al. 2010, A&A, 517, A22
Mosser, B., Goupil, M. J., Belkacem, K., et al. 2012a, ArXiv e-prints 1209.3336
Mosser, B., Goupil, M. J., Belkacem, K., et al. 2012b, A&A, 540, A143
Mosser, B., Michel, E., Belkacem, K., et al. 2013, submitted to A&A
Osaki, Y. 1975, PASJ, 27, 237
Ouazzani, R.-M., Dupret, M.-A., & Reese, D. 2012, ArXiv e-prints
Reese, D., Lignières, F., & Rieutord, M. 2006, A&A, 455, 621
Samadi, R., Belkacem, K., Dupret, M.-A., et al. 2012, A&A, 543, A120
Scuflaire, R. 1974, A&A, 36, 107
Shibahashi, H. 1979, PASJ, 31, 87
Tassoul, M. 1980, ApJS, 43, 469
Unno, W., Osaki, Y., Ando, H., Saio, H., & Shibahashi, H. 1989, Nonradial oscillations of stars, Tokyo: University of Tokyo Press, 1989, 2nd ed.

Appendix A: Properties of eigenfunctions and mode inertia

A.1. Displacement eigenfunctions

The displacement eigenfunctions computed for two modes of the selected pattern (see Table 2) for model M1 are shown as a function of the normalized radius r/R in Fig. A.1. They correspond to the modes with the largest and smallest maximum amplitudes in the pattern. The inner part is dominated by the horizontal displacement z_2 and oscillates with a large number of nodes, typical of a high-order gravity-mode. The largest maximum amplitude corresponds to the most g-dominated mode whereas the smallest maximum amplitudes arise for the p-m modes ν_1 and ν_6.

The maximum amplitude of z_2 occurs deep in the g-cavity, at the same radius for all modes of the pattern. The region of non-negligible amplitude defines the radius of a *seismic rotating core* which is found here independent of the mode ($r/R \sim 0.02$) and far smaller than the upper turning radius of the inner gravity resonant cavity ($x_2 \sim 0.08$, Table 3)

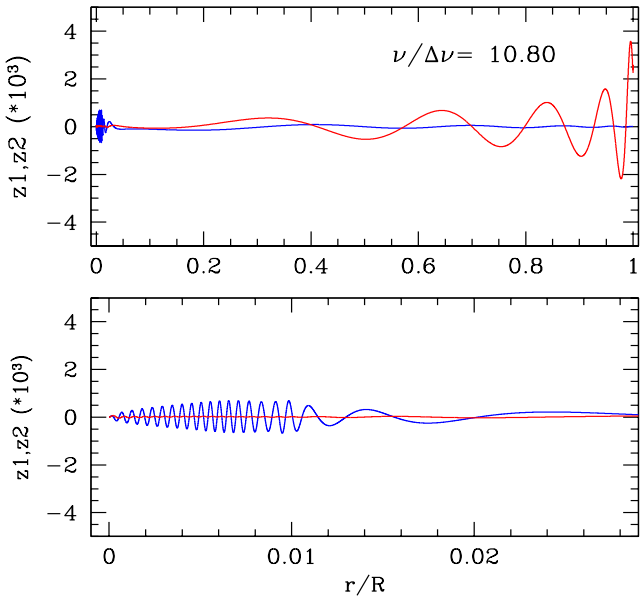

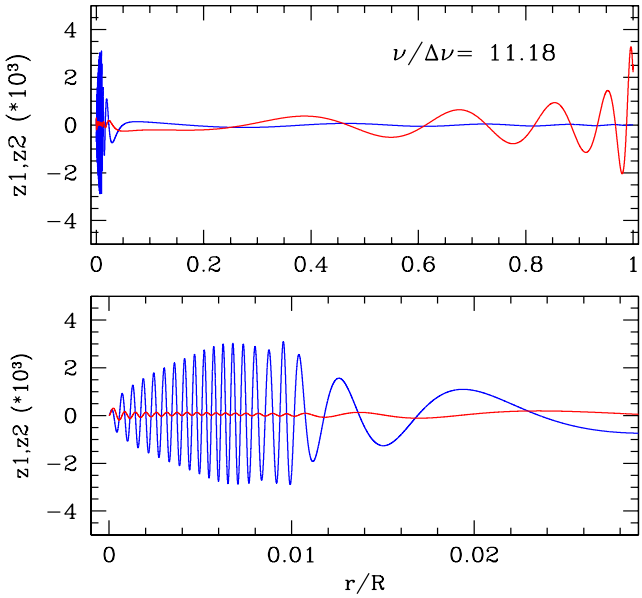

Fig. A.1. Displacement eigenfunctions as a function of the normalized radius r/R, in blue the horizontal component to the displacement eigenfunction z_2 (Eq. 7) and in red the radial component to the displacement eigenfunction z_1 (Eq. 6). From top to bottom $\ell = 1$ modes 1 and 3 of Table. 2.

A.2. Behavior of β and $\beta_{\rm core}$ with ζ

For $\ell = 1$ modes of red giants, the term $z_2 z_1$ in β (Eq. (13)) plays almost no role because $z_2 z_1 \ll z_2^2$ in the core and $z_2 z_1 \ll z_1^2$ in the envelope (see Fig. A.1). As a result, we have

$$\beta \approx \frac{1}{I}\int_0^1 \left(z_1^2 + z_2^2 - \frac{1}{2}\,z_2^2\right)\,\frac{{\rm d}x}{x} \tag{A.1}$$

$$= 1 - \frac{1}{2}\,\frac{1}{I}\int_0^1 z_2^2\,\frac{{\rm d}x}{x} \tag{A.2}$$

$$= 1 - \frac{1}{2}\zeta\,. \tag{A.3}$$

where ζ is defined in Eq.10. The linear dependence of β with ζ is verified in Fig. A.2. Furthermore, for all modes, $z_2^2 \gg z_1^2$, $2 z_1 z_2$ in the g- cavity (see Fig.A.1) then $\beta_{\rm core,nl} \approx \beta_{\rm core}$ where for $l = 1$ modes, we derive

$$\beta_{\rm core} \approx \frac{1}{I}\int_{\rm core} \left(z_1^2 + z_2^2 - \frac{1}{2}\,z_2^2\right)\,\frac{{\rm d}x}{x} \tag{A.4}$$

$$\approx \frac{1}{2I}\int_{\rm core} z_2^2\,\frac{{\rm d}x}{x} = \frac{1}{2}\,\frac{I_{\rm core}}{I} = \frac{1}{2}\,\zeta\,, \tag{A.5}$$

hence

$$\beta_{\rm env} = \beta - \beta_{\rm core} \approx 1 - \zeta\,. \tag{A.6}$$

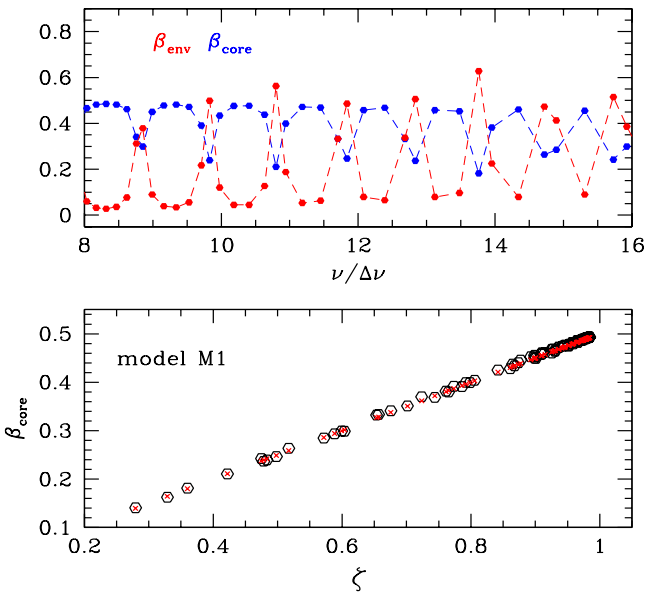

Fig. A.2. *Top:* $\beta_{\rm env}$ and $\beta_{\rm core}$ as a function of $\nu/\Delta\nu$ for model M1. *Bottom* Same as top for the ratio $\beta_{\rm core}$ as a function of ζ (black open dots). The approximation $\beta = 1-(1/2)\,\zeta$ using the numerical values of ζ is represented with red crosses.

Numerical values for model M1 confirm that $\beta_{\rm core}$ increases linearly with ζ with a slope 1/2 (Fig. A.2). For g-m modes ($\zeta \sim 1$), $\beta_{\rm core}$ dominates with a nearly constant value of 0.5. P-m modes correspond to the *teeth* of the saw type variation of β_{env} and the ratio $\beta_{\rm env}/\beta_{\rm core} \sim 0.25$ (Fig. A.2).

A.3. An approximate expression for ζ

This section determines an approximate expression of $\zeta = I_{\rm core}/I$ as a function of $\nu/\Delta\nu$. The derivation is based on results of an asymptotic method developed by Shibahashi (1979) to which we refer for details (see also Unno et al. 1989).

– The envelope (∼p-propagative cavity) is characterized by $z_2^2 \ll z_1^2$. Using Eq. (16.47) from Unno et al., it is straightforward to derive the following approximate expression

$$z_1^2\,\frac{{\rm d}x}{x} \sim \frac{c^2}{\sigma}\left(1-\sin\sigma\tau\right)\,{\rm d}\tau\,. \qquad (A.7)$$

The constant c can be determined by the condition $\xi_{\rm r} = 1$ at the surface.

$$\tau(x_3,x) = \frac{2}{\sigma}\int_{x_3}^{x} k_{\rm r}\,{\rm d}x'\,, \qquad (A.8)$$

with

$$k_{\rm r} \sim \frac{1}{c_s}\left(\sigma^2 - S_l^2\right)^{1/2}. \qquad (A.9)$$

where we have assumed $\sigma^2 >> N^2$ in Eq.27. Note that in the process of deriving the amplitude of z_1^2 arising in front of the sinusoidal term in Eq.A.7, one can neglect S_l^2 in front of σ^2 in the expression for $k_{\rm r}$ (i.e. $k_{\rm r} \sim \sigma/c_s$). However this is not the case when $k_{\rm r}$ is in the phase of the sinusoidal term where we keep the expression Eq.A.9.
The inertia in the envelope can then be approximated as:

$$I_{\rm env} \sim \int_{\rm env} z_1^2\,\frac{{\rm d}x}{x} \qquad (A.10)$$

$$\sim \frac{c^2}{\sigma}\tau_p\,\left(1-\frac{\cos(\sigma\tau_p)-1}{\sigma\tau_p}\right) \sim \frac{c^2}{\sigma}\,\tau_p\,, \qquad (A.11)$$

where we have defined

$$\tau_p = \frac{2}{\sigma}\int_{x_3}^{1}\left(\sigma^2-S_l^2\right)^{1/2}\frac{{\rm d}x}{c_s} = \frac{2\pi}{\sigma}\,\frac{1}{f}\,\frac{\nu}{\Delta\nu}\,, \qquad (A.12)$$

and the mean large separation is

$$\Delta\nu \equiv \left(2\int_0^1 \frac{{\rm d}x}{c_s}\right)^{-1}. \qquad (A.13)$$

The factor f is of order unity and represents the difference between the integration from x_3 and from the center. We take $f = 1$ unless specified otherwise. The last equality in Eq. (A.11) is obtained assuming $\sigma\tau_p \gg 1$.

– The core (∼g-propagative cavity) is characterized by $z_2^2 \gg z_1^2$. Again, the asymptotic results lead to the following expression

$$z_2^2\,\frac{{\rm d}x}{x} \sim \frac{a^2}{\sigma}\left(1-\sin\sigma\tau\right)\,{\rm d}\tau\,, \qquad (A.14)$$

where a is a constant that is determined by the resonant frequency condition between the p and g cavities and

$$\tau(x_1,x) = \frac{2}{\sigma}\int_{\rm x_1}^{x} k_{\rm r}\,{\rm d}x'\,, \qquad (A.15)$$

and we have used

$$k_{\rm r} \sim \frac{\sqrt{\Lambda}}{\sigma x}\,(N^2-\sigma^2)^{1/2}\,. \qquad (A.16)$$

Hence recalling that $\sigma\tau_g \gg 1$, the inertia in the core can be approximated as

$$I_{\rm core} \sim \frac{a^2}{\sigma}\,\tau_g\,\left(1+\frac{\cos(\sigma\tau_g)-1}{\sigma\tau_g}\right) \sim \frac{a^2}{\sigma}\,\tau_g\,, \qquad (A.17)$$

where we have defined

$$\tau_g = \tau(x1,x2) = \frac{\sqrt{\Lambda}}{\sigma^2}\int_{\rm core}(N^2-\sigma^2)^{1/2}\,\frac{{\rm d}x}{x}\,. \qquad (A.18)$$

– The ratio $q \equiv I_{\rm env}/I_{\rm core}$ is then approximated by

$$q \approx \left(\frac{c}{a}\right)^2\,\frac{\tau_p}{\tau_g}\,. \qquad (A.19)$$

– We obtain the ratio c/a (from Unno et al's Eq. (16.49) and Eq. (16.50)) as

$$\frac{c}{a} = 2\,\frac{\cos(\sigma\tau_g/2)}{\cos(\sigma\tau_p/2)} \sim \pm 2\,\cos\left(\frac{\sigma\tau_g}{2}\right)\,, \qquad (A.20)$$

where we have used the fact that $\sigma\tau_p \sim 2n_p\pi$. A exponential term is present in Unno et al's expression with the argument being an integral over the evanescent region between the p- and g-cavities. As this region is quite narrow in our models for the considered modes, the exponential is taken to be 1. Nevertheless the width of the evanescent region depends on the considered mode and in some cases, for accurate quantitative results, it might be necessary to include effects of the evanescent zone with a finite width.

– The ratio q is then eventually approximated by

$$q \;=\; 4\;\cos^2\Big(\frac{\sigma\tau_g}{2}\Big)\;\frac{\tau_p}{\tau_g}\,. \tag{A.21}$$

– For the relative core inertia $\zeta = I_{\rm core}/I$,

$$\zeta = \frac{1}{1+q} \approx \Big(1+4\;\cos^2\Big(\frac{\sigma\tau_g}{2}\Big)\;\frac{\tau_p}{\tau_g}\Big)^{-1}\,. \tag{A.22}$$

– We now use the approximate expressions Eq. (A.12) and Eq. (A.18) in order to derive for the ratio τ_p/τ_g in terms of observable quantities

$$\frac{\tau_p}{\tau_g} \approx \frac{1}{f}\;\alpha_0\;y^2\,, \tag{A.23}$$

where for convenience we hase defined $y = \nu/\Delta\nu$ and

$$\alpha_0 \;=\; \Delta\nu\;\Delta\Pi\,, \tag{A.24}$$

with the period spacing for g modes

$$\Delta\Pi \;=\; \frac{2\pi^2}{\sqrt{\Lambda}}\;\left(\int_{\rm core}\;(N^2-\sigma^2)^{1/2}\,\frac{{\rm d}x}{x}\right)^{-1}\,. \tag{A.25}$$

We also write

$$\sigma\tau_g = \;\frac{2\pi}{\Delta\Pi\;\nu}\,, \tag{A.26}$$

so that we obtain

$$\zeta \;\approx\; \frac{1}{1+\alpha_0\;\chi^2/f} \approx \frac{1}{1+\alpha_0\;\chi^2} \tag{A.27}$$

$$\chi \;=\; 2\;\frac{\nu}{\Delta\nu}\;\cos\Big(\frac{\pi}{\Delta\Pi\;\nu}\Big)\,. \tag{A.28}$$